Earthquake Focal Mechanisms and Principal Stress Orientation in Long Valley Caldera,

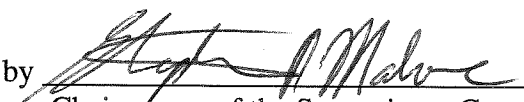California: June 1997-September 1997

by Gillian Sharer

A thesis submitted in partial fulfillment
of the requirements for the degree of

Master of Science

University of Washington

1998

Approved by _____
Chairperson of the Supervisory Committee

Program Authorized
to Offer Degree_____

Date_____

Master's Thesis

In presenting this thesis in partial fulfillment of the requirements for a Master's degree at the University of Washington, I agree that the Library shall make its copies freely available for inspection. I further agree that extensive copying of this thesis is allowable only for scholarly purposes, consistent with "fair use" as prescribed in the U.S. copyright law. Any other reproduction for any purposes or by any means shall not be allowed without my written permission.

Signature _Gillian Sharer_

Date _8/4/98_

BINDERY INFORMATION

of Thesis __1__   Color: __Black (990)__   Color Stamping: __Gold__   Year: __1998__

Please check one:

__X__ Standard cover and spine stamping

_____ Nonstandard (note special instructions below)

Note: This thesis contains (check if applicable)

_____ Pockets _____ Foldouts _____ Overlays

Earthquake Focal Mechanisms and
Principal Stress Orientation in
Long Valley Caldera, California:
June 1997 – September 1997

Earthquake Focal Mechanisms and Principal Stress Orientation in Long Valley Caldera, California: June 1997-September 1997

by Gillian Sharer

5   20mmi   44J
1/99 31364-144 NULB

TH

ThesisBinding   1/97

*71440

University of Washington

Abstract

Earthquake Focal Mechanisms and Principal Stress Orientation in Long Valley caldera,
California: June 1997-September 1997

by Gillian Sharer

Chairperson of the Supervisory Committee
Professor Stephen D. Malone
Geophysics Program

Long Valley caldera has shown signs of unrest since 1980 in the forms of increased seismic swarms and deformation. This study investigates the uniformity of stress in this region using earthquake focal mechanisms. High quality focal mechanisms were obtained using P-wave polarity data from 696 earthquakes located in the south moat of the caldera and in the Sierran block just south of Long Valley. These focal mechanisms were inverted for a best fit stress orientation using Gephart and Forsyth's (1984) stress inversion technique. The inversion of the entire data set produces a best fit uniform stress direction for which the maximum principal stress (σ_1) is oriented 315° with a plunge of 40°, and the minimum principal stress (σ_3) is oriented 217° with a plunge of 17°. Inversions of earthquake subsets show statistically significant differences in stress orientations between earthquakes clustering in the eastern and western sections of the south moat. While the trends of the best fit σ_1 are similar between the two subsets, there is a difference in plunge of 50°. The west group demonstrates a pure-strike slip faulting regime with an almost horizontal σ_1, while the east group demonstrates a faulting regime which is midway between strike-slip and normal faulting (σ_1 plunges 45°). The best fit stress orientation in the south Sierran block subset is rotated towards what is typically thought of as east-west Basin and Range extension. However, this result is not statistically significant. While variations in stress orientation exist in the south moat, they do not appear to show evidence for a radial stress influence from a magma chamber beneath the resurgent dome.

TABLE OF CONTENTS

LIST OF FIGURES

LIST OF TABLES

ACKNOWLEDGEMENTS

Introduction

Long Valley caldera is a volcanic system in eastern California which has experienced increased seismicity and deformation since 1980, possible precursors to renewed volcanic activity. However, especially for large caldera systems, periods of unrest may last for decades prior to renewed volcanism or they may cease with no surface expression of volcanism (Newhall and Dzurisin, 1988). This period of unrest at Long Valley offers an opportunity to better understand the natural history of unrest at these systems.

Interaction of tectonic and magmatic processes determines the distribution of stress in a volcanic region. The purpose of this study is to investigate the distribution of stress at Long Valley caldera as determined by earthquake focal mechanisms. Earthquake focal mechanisms contain information about slip direction on a fault which in turn constrains the orientation of stress acting on the fault. In this study, I use the stress inversion technique of Gephart and Forsyth (1984) to invert the focal mechanisms for a uniform stress direction.

Questions which I address are: Can the stress field at Long Valley be distinguished from a uniform stress using this technique? Do focal mechanisms provide evidence for a rotation of the stress field radial to an inflation source central to the resurgent dome of the caldera? Do modeled fault planes provide any information about the structure of the south moat at Long Valley? This study is constrained to focus on the south moat of the caldera due to the distribution of the earthquakes (Figure 1). This distribution limits the attempt to find radial variation in stress using focal mechanisms. However, if the stress field is

strongly influenced by a local radial stress, nonuniformity of the stress field should be

evident.
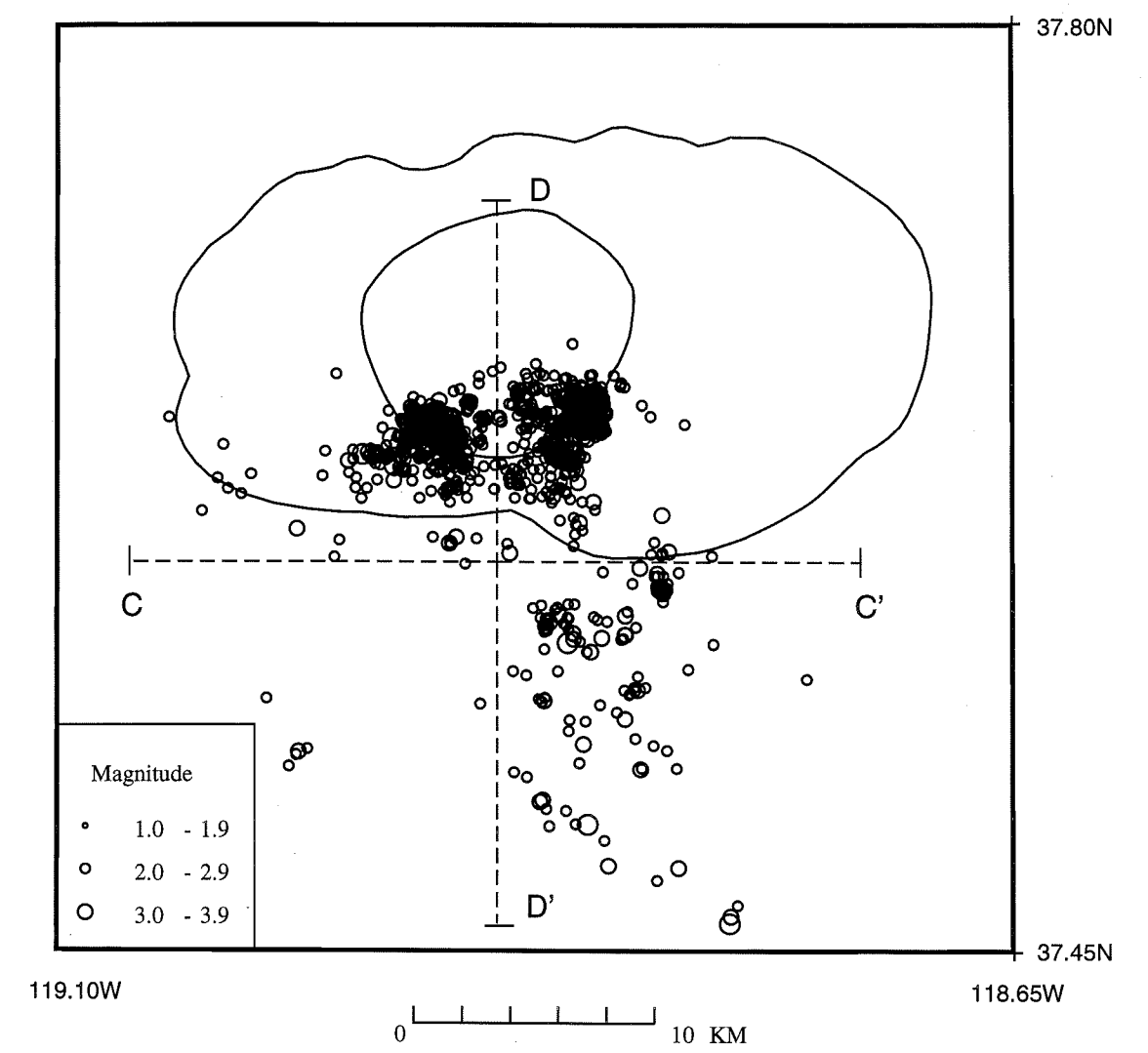
Figure 1: Map of all earthquakes in Long Valley area that have magnitudes greater than or equal to 1.0, June-September 1997. The caldera and resurgent dome boundaries are outlined. Cross-sections shown in Figure 8 are indicated by the dashed lines (C-C', D-D').

Chapter 1

Geologic Structure and History of Long Valley

Long Valley caldera, California is an east-west elongated volcanic collapse feature which formed ~0.7 Ma during a massive eruption which ejected greater than 600 km^3 of rhyolitic material (Bailey, 1976). It shares many features of typical calderas including steep walls, a moat structure, and a central resurgent dome. An active hydrothermal system feeds hot springs and occasional geyser activity in the area (Bailey, 1976). Situated on the eastern edge of the Sierra Nevada province and influenced by Basin and Range extension, Long Valley caldera is intersected by northwest trending Sierran front normal faults and regional graben features (Bailey, 1976, Bailey, 1989) (Figure 2). Although currently active (the Hilton Creek fault has had 25 m of offset in the past 11,000 years (Rundle and Hill, 1988)), these faults are not continuous across the moat structure. Surficial faulting within the caldera is dominated by a northwest trending graben structure across the resurgent dome (Bailey, 1976). The subsurface structure consists of shallow volcanic material, glacial material, and lake deposits overlying approximately 1 km of volcanic tuff from the caldera-forming eruptions. Depths to Sierran granite basement rocks underlying the caldera range from 1.5 to 3 km (Hill et al., 1985b).

Long Valley caldera is intersected along its western edge by a much younger and more recently active volcanic structure, the Mono-Inyo volcanic chain. This north-trending linear chain of trachybasaltic to rhyolitic domes extends from Mammoth Mountain, a

cumulovolcano located just southwest of Long Valley caldera, northward for 40 km to Mono Lake (Bailey, 1976).

Volcanic activity began in this region approximately 3.6 Ma with eruptions of trachybasaltic-trachyandesitic material (Bailey, 1976). By 2.1 Ma, a large, shallow differentiated magma chamber had developed which led to rhyolitic eruptions from Glass Mountain, located on the north-eastern edge of the present caldera. Since the caldera forming eruptions of 0.7 Ma, major eruptions from the caldera system have occurred at approximately 200,000 year intervals with the last episode occurring 0.1 Ma. These eruptions typically vented from the moat structure, presumably along a ring fracture system (Bailey, 1976).

The most recent volcanic activity has been confined to the Inyo-Mono craters system. Trachybasaltic-trachyandesitic eruptions began along this system 0.2 to 0.3 Ma and appear to have propagated northward along a dike structure, though the entire system remains active (Bailey, 1976, Fink, 1985). Younger material from this system is generally (but not exclusively) rhyolitic in composition. These eruptions are usually small, forming numerous dome structures. Their recurrence interval is approximately 500 to 600 years with the most recent eruptions of rhyolitic material occurring 650 to 550 years ago (Miller 1985, Sieh and Bursik, 1986). Mammoth Mountain itself formed by repeated eruptions from this system over a period of time from 200 ka to 50 ka (Bailey, 1976).

Recent Activity: Seismicity and Deformation

The region around Long Valley began showing an increase in seismicity in 1978 with a magnitude 5.6 earthquake located 20 km south of the caldera (Ryall and Ryall, 1981). The area south of the caldera remained seismically active and in 1980 four magnitude 6 earthquakes occurred within days of each other. One of these earthquakes was located within the southern moat of the caldera, an area which has since been subject to earthquake swarms of varying intensity (Rundle and Hill, 1988). Much of the seismic activity within the caldera has occurred in the south moat, while seismicity outside the caldera is concentrated in the Sierran block south of the caldera. This spatial distribution of seismicity can be seen in Figure 3, which shows all earthquakes with a local magnitude greater than 3.0 that occurred between 1978 and 1996. Notably, the south moat swarm of January 1983 included magnitude 5.2 and 5.4 earthquakes and thousands of smaller earthquakes over a period of several days (Savage and Cockerham, 1984). Smaller south moat swarms occur frequently.

A swarm of small earthquakes also occurred near Mammoth Mountain, southwest of the caldera, in late 1989 (Hill et al., 1990). This swarm is notable for marking the beginning of low frequency earthquakes beneath Mammoth Mountain (Hill et al., 1990) and for its probable association with increased levels of CO_2 in the soil of several areas near Mammoth Mountain (Farrar et al., 1995). Low frequency earthquakes are frequently seen in active volcanic systems and are commonly associated with movement of magma. Because of the presence of CO_2 and low frequency earthquakes, along with increased

seismicity and deformation, it is likely that the Mammoth Mountain swarm was directly associated with the emplacement of a dike (Hill et al., 1990). It is less clear what relationship the south moat swarms have to volcanic activity, although dike emplacement has been suggested (Savage and Cockerham, 1984).

Inflation across the resurgent dome has accompanied the increase in seismicity. Since 1978, the dome has risen more than 50 cm, at rates generally of 2-3 cm/yr (Hill et al., 1990). However, deformation has been episodic and much larger rates of uplift have occurred over short periods of time. This expansion has been mostly radially symmetric and aseismic, with intra-caldera seismicity most often confined to the south moat (Langbein, 1993). Many attempts have been made to model this deformation (e.g. Savage and Cockerham 1987, Langbein et al., 1993, Estrem et al., 1985, Rundle and Whitcomb, 1984). Much of the inflation from 1979-1982 can be modeled satisfactorily with a single expanding point source, representing a physical magma chamber, at depths of 7-10 km beneath the central resurgent dome. However, since 1983, the deformation seems to require a modification to this model, possibly with a second inflation source beneath the south moat combined with right lateral slip on east-west striking faults in the south moat (Denlinger et al., 1987, Langbein, 1989, Savage et al., 1987). The relative contributions from each of these proposed sources changes with time, indicating spatial as well as temporal variability in the processes occurring at Long Valley. In 1989, deformation preceded a south moat seismic swarm by several months indicating some influence of the magmatic system on the earthquake activity (Langbein, 1993), possibly as a direct source of stress or as a trigger. Such triggering may occur as stress from the magmatic system

loads faults which are very close to failure, or as heat causes an increase in pore pressure thereby lowering the friction along faults (Newhall and Dzurisin, 1988).

A previous attempt at defining the stress field in Long Valley was made by Moos and Zoback (1993). Inverting 29 focal mechanisms in the south moat for stress orientation, they find a strike-slip regime with a maximum stress axis oriented to the north-west and a minimum stress axis oriented to the south-west. Stress resulting from a magma chamber beneath the resurgent dome was modeled by Wu and Wang (1988). They conclude that a spherical magma chamber with a 5 km diameter whose top was located at 7 km depth would have a negligible effect on stress in the south moat, while an elliptical magma chamber would make a larger contribution to the stress in the south moat. In this study, I attempt to determine whether the inflation source beneath the south moat has a discernible effect on the local stress field by testing the hypothesis that the stress field in the Long Valley region is uniform. A uniform stress field would suggest that a regional stress dominates in this area. If stress from a magma chamber has a strong influence on the occurence of these earthquakes, one might expect to see a variation in the stress field radial to the resurgent dome, with the maximum compressional axes rotated towards the resurgent dome.
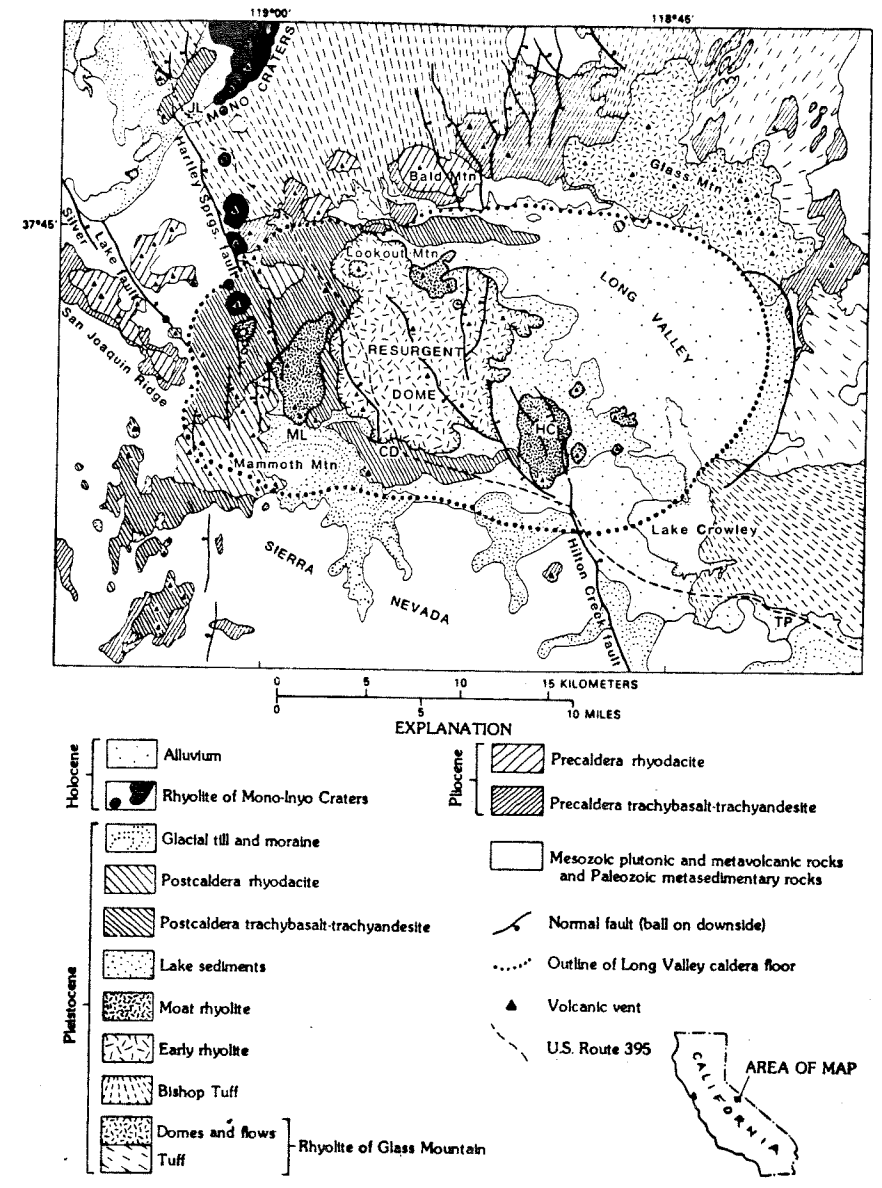
Figure 2: Geologic map of Long Valley caldera. JL, June Lake; ML, Mammoth Lakes, CD, Casa Diablo; HC, Hot Creek; TP, Toms Place [from Bailey et al. (1989)].
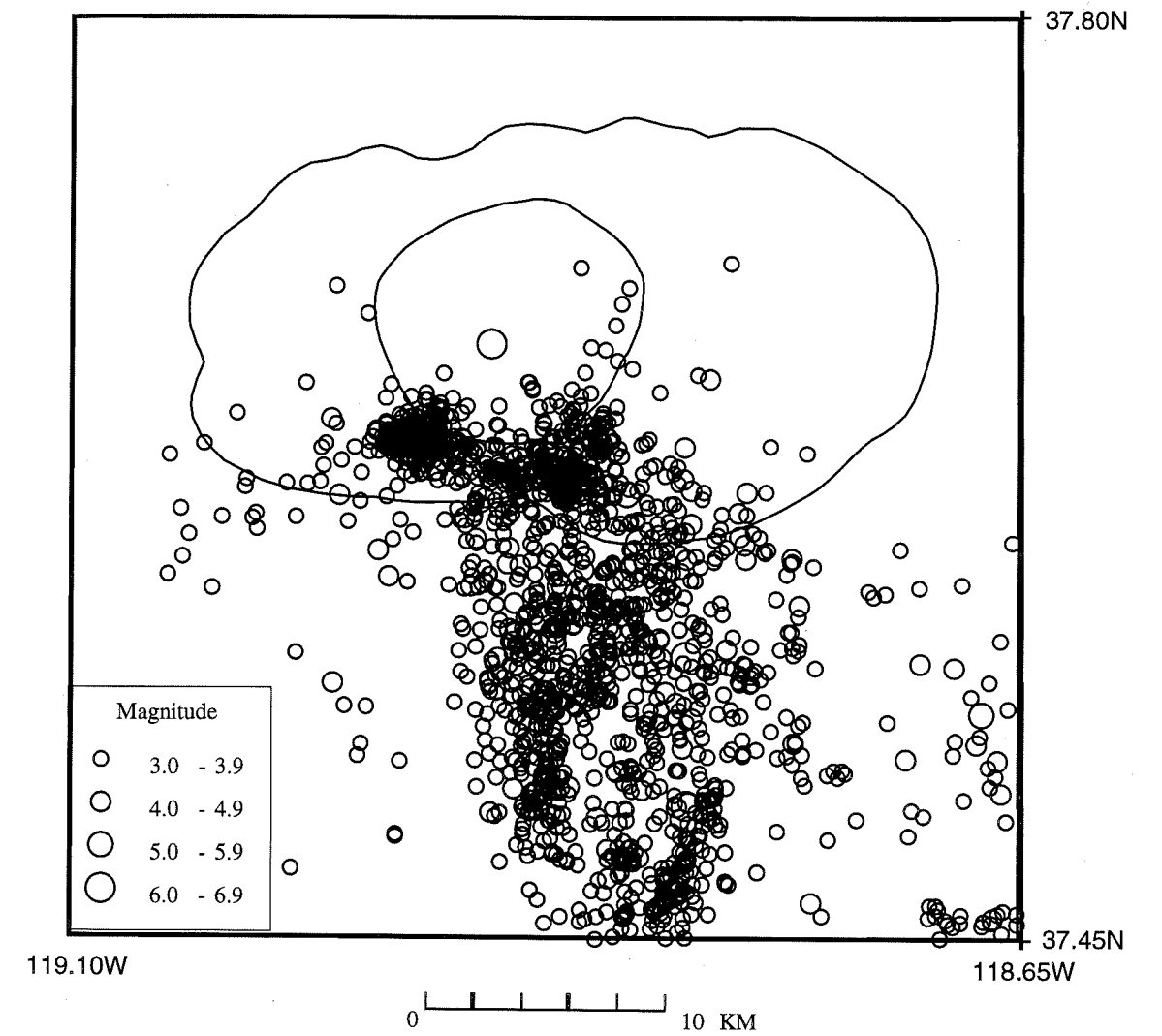
Figure 3: Map of all earthquakes with a magnitude of 3.0 or greater located near Long Valley caldera, 1978-1996.

Chapter 2

Data Sources

The data that I use in this study derive from three sources: the Duke University Seismology Group, the Northern California Earthquake Data Center, and the U.S. Geological Survey/Durham University, England. All of these sources provided catalogs and/or waveforms of earthquakes occurring in and around Long Valley caldera during the summer of 1997. Figure 4 illustrates the locations of seismic stations which recorded at least one phase used in this study. During the summer of 1997, these seismic networks densely covered the region.

Duke University Seismology Group:

The Duke University seismology group, under the direction of Dr. Peter Malin, maintained a temporary seismic array in Long Valley Caldera from May 1997 through September 1997. This array consisted of 42 three-component 2-Hz L22 seismometers and 4 Guralp broadband instruments recording in triggered mode at 500 samples per second on Reftek data loggers. For this study, I used arrival times of P- and S-phases and polarities of P-phases picked by Dr. Peter Malin's seismology group. This data set provides the majority of phases (68.6%) used in focal mechanism determination.

Northern California Earthquake Data Center (NCEDC):

I use arrival times and polarity picks of hand-picked P-phases contained in the Northern California Earthquake Catalog which is made available by the Northern California Seismic Network, U.S. Geological Survey, Menlo Park, and the Seismological Laboratory, University of California, Berkeley. The Northern California Seismic Network has 19 permanent short-period stations located within 20 km of the caldera and 13 more stations located within 50 km of the caldera. 31.1% of the phase picks used in my final data set derive from this source.

U.S. Geological Survey/ Durham University, England:

Dr. Bruce Julian, of the U.S. Geological Survey, in collaboration with Dr. Gillian Foulger, of Durham University, England, operated a temporary seismic array in Long Valley Caldera which was run concurrently with the Duke University array. This array consisted of 23 3-component 2-Hz L22 seismometers and 2 Guralp broadband instruments run in continuous mode at 100 samples per second. This data source provides a small portion of my overall data set (0.3%). I hand-picked arrival times and polarities of P-phases from waveforms recorded on August 2, 1997. Thirteen events occurring on this date were included in my final data set.

Data Selection

I began assembling my data set by obtaining the earthquakes in the NCEDC catalog

with a magnitude greater than 1.0 located within a square region centered on Long Valley caldera and bounded by 37.4°N, 38.0°N latitude and 119.3°W, 118.5°W longitude. NCEDC phase picks were included if they were hand-picked and assigned a good quality code (0 or 1, based on uncertainties in phase arrival time). These phase picks were combined with phase picks from the Duke catalog if their respective earthquake origin times were within 1.5 seconds of each other. These picks were initially assumed to be from the same earthquake, with the difference in origin times assumed to be primarily due to differences in velocity models used for locating the earthquakes. The Duke phase picks also met the criteria of being hand-picked with a good quality code. I subsequently relocated the earthquake using both sets of picks and a layered modification of the Northern California gradient velocity model MAM (Table 1). For this relocation, I used equal weighting for all the NCEDC and Duke P-phase picks because of apparent differences in weighting styles between the two catalogs. Duke S-phase picks with an assigned quality of 0 to 2 were also used in the relocation. Station corrections associated with the Northern California velocity model MAM were retained. When using only NCEDC picks, Northern California station corrections improved the agreement between locations determined by the velocity model MAM and my modified velocity model. Independent determination of station corrections was not attempted, and Duke stations were not assigned any corrections.

Of 1937 earthquakes whose picks could be merged between the two catalogs, 1580 earthquakes were relocated with a quality code of BB or better. This quality code signifies that the root-mean-square residual (RMS) of the origin time is less than 0.3 seconds, the

horizontal error is less than 2.5 km, the vertical error is less than 5 km, and the spatial distribution of stations is such that there is no azimuthal gap greater than 135°. Of these earthquakes, 38 were not used because the location program fixed their depth in order to complete the inversion. Given the density of stations in the area, earthquakes which cannot be located well might indicate either a location at the edges of the dense array or an incorrect merging of the data sets (i.e. a combination of picks from separate events placed into one file). Either of these scenarios could produce of a poor focal mechanism and the earthquakes which could not be located with a quality of BB or better were thrown out from further use. In the final data set of good focal mechanisms, discussed in more detail in the following section, more than 85% of the earthquakes had location qualities of AA, which allows for an RMS of less than 0.15 seconds, a horizontal error of less than 1 km, a vertical error of less than 2 km, and a station distribution gap of less than 90°.

Comparing my locations with those of both the Duke Seismology Group and the NCEDC, I find that differences in location are generally small. Differences between my locations and those of Duke are generally less than 1 km in horizontal distance and 1.5 km in depth. Differences between my locations and those of the NCEDC are slightly larger; The large majority of earthquake locations are within 1.5 km horizontally and 2.5 km vertically. Location differences of this magnitude do not affect the focal mechanism solutions.

Focal mechanisms were calculated using the U.S. Geological Survey program FPFIT (Reasenberg and Oppenheimer, 1985), which fits focal planes to P-wave polarity data. This program constrains the mechanisms to be double-couple and performs a grid search

over the available solution space. This assumption of double-couple solutions may not be valid for some of the earthquakes in Long Valley (Julian, 1985). However, all of the focal mechanisms used in this study are at least consistent with a double-couple solution, although other non-double couple solutions may not be always precluded. Multiple solutions are reported by FPFIT if two or more solutions are of similar quality, and earthquakes with multiple focal mechanism solutions were not used in the stress inversions. For the calculation of focal mechanisms, all polarity picks retain their equal weighting. The quality of the resulting solutions is determined through the use of three measures, α, δ, and r. α is a quantity which describes the one-norm misfit between the actual polarities and the polarities predicted by the focal mechanism solution (0.00 being a perfect fit, 1.00 being a perfect misfit). δ is the largest uncertainty in the strike, dip, or rake of the solution. This uncertainty is calculated by assuming that α is normally distributed, constructing its 90% confidence interval, and searching for the largest variation in strike, dip, and rake of solutions which span this confidence interval. r is the station distribution ratio, describing the location of the polarity picks relative to the nodal planes. In practice, r is calculated as the average of the square-root of the normalized theoretical P-wave radiation amplitude for the modeled focal mechanism at each station, such that $r = 0.0$ indicates that all the stations lie on nodal planes (and have theoretical zero amplitudes) while $r = 1.0$ indicates that all the stations lie at points of maximum amplitude. For acceptable focal mechanisms, I constrain r to be greater than or equal to 0.40 and the number of phase picks to be greater than or equal to 15. These constraints increase the likelihood that the focal sphere is adequately sampled. In assigning quality

codes to the resultant FPFIT focal mechanisms, I follow the criteria of Gillard, Wyss, and Okubo (1996). This scheme is as follows:

A: $0.00 \leq \alpha \leq 0.07$ and $0^{o} \leq \delta \leq 10^{o}$

B: $0.00 \leq \alpha \leq 0.07$ and $10^{o} < \delta \leq 20^{o}$ or, $0.07 \leq \alpha \leq 0.14$ and $0^{o} \leq \delta \leq 20^{o}$

C: $0.14 \leq \alpha \leq 0.20$ and $\delta \leq 20^{o}$ or, $0.00 \leq \alpha \leq 0.20$ and $20^{o} < \delta \leq 30^{c}$

D: $0.00 \leq \alpha \leq 0.20$ and $30^{o} < \delta$ or, $\alpha > 0.20$

Of the 1336 earthquakes with single focal mechanism solutions reported by FPFIT, 696 satisfy the criteria for qualities A or B. In an attempt to reduce the possible errors present in the data set, focal mechanisms with assigned qualities of C or D were not included in the final set of focal mechanisms. 132 quality A and 564 quality B earthquakes comprise the data set which I use to invert for crustal stress orientation. They have an average of 30 polarity picks. While the average α statistic is 0.02, over 50% of the earthquakes have an α statistic of 0.00. The average r value is 0.6 and the average δ statistic is 17°. These focal mechanism solutions are of very high quality. This quality is illustrated in Figure 5 which presents a randomly selected group of focal mechanisms from my data set. The majority of these mechanisms are unambiguously double-couple.

Description of data set

The earthquake focal mechanisms used for the stress inversions consist of 80% strike

slip faulting, 11% reverse faulting, and 9% normal faulting mechanisms. Of these solutions, 44% have significant oblique components. In map view (Figure 6), the majority of earthquakes occur in two diffuse areas, both in the south moat. One group of earthquakes is located on the southwest boundary of the resurgent dome; the other is located on the southeast boundary of the resurgent dome. In cross-section (Figure 7), the western group appears to dip slightly to the west, while the eastern group has a more noticeable eastern dip. While the two groups are similarly dominated by strike-slip faulting, the western group contains 80% (61 / 77) of the reverse mechanisms. A small percentage of earthquakes are located in the region south of the caldera. Due to the configuration of the network, combined with the strict criteria for acceptable focal mechanisms, these earthquakes have a higher proportion of larger events than the earthquakes within the caldera. The majority of earthquakes are located at depths of 3-9 km, with the shallower earthquakes concentrated in the south moat region. Earthquakes outside of the caldera tend to be deeper than 5 km (Figure 7). These spatial features of my data set are representative of the seismicity of all well located earthquakes with a magnitude greater than or equal to 1.0 in this region (Figure 7, Figure 8). Figure 9 illustrates the P-and T-axes calculated for each of the 696 focal mechanisms. The P-axes tend to group in the northwest quadrant of the stereonet while the T-axes predominate in the southwest quadrant.

Table 1: layered velocity model used for earthquake relocations

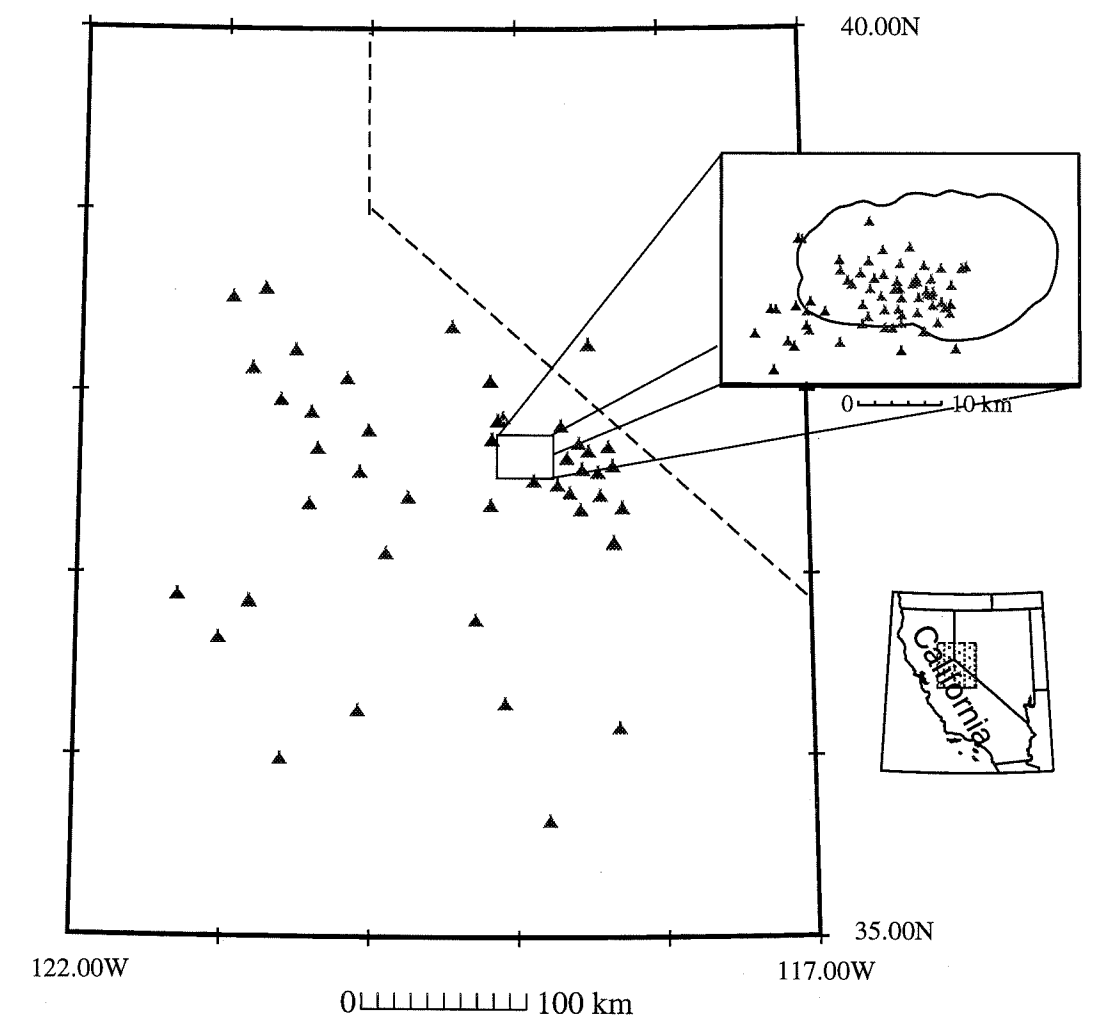| depth (km)	velocity (km/sec)
0.0	3.52
1.3	3.67
1.8	4.29
2.3	4.91
2.8	5.53
4.2	5.70
5.6	5.87
7.0	6.03
29.0	6.28

Figure 4: Locations of seismic stations (shown by triangles) which contributed at least one phase to my data set. The dashed line indicates the California-Nevada border.

9706220818
D= 2.60   M=1.2

9706291659
D= 2.98   M=1.1

9709070032
D= 4.05   M=1.0

9707120507
D= 5.37   M=1.2

9707290659
D= 4.97   M=1.2

9707300149
D= 4.08   M=1.8

9707300751
D= 4.31   M=1.4

9707301324
D= 6.57   M=2.1

9707302249
D= 6.76   M=1.6

9708032135
D= 4.89   M=1.6

9708151429
D= 5.49   M=1.1

9708180827
D= 7.43   M=2.1

9709070032
D= 4.05   M=1.0

9709151934
D= 6.90   M=1.5

9709170628
D= 6.73   M=1.9

9709211614
D= 6.63   M=2.1
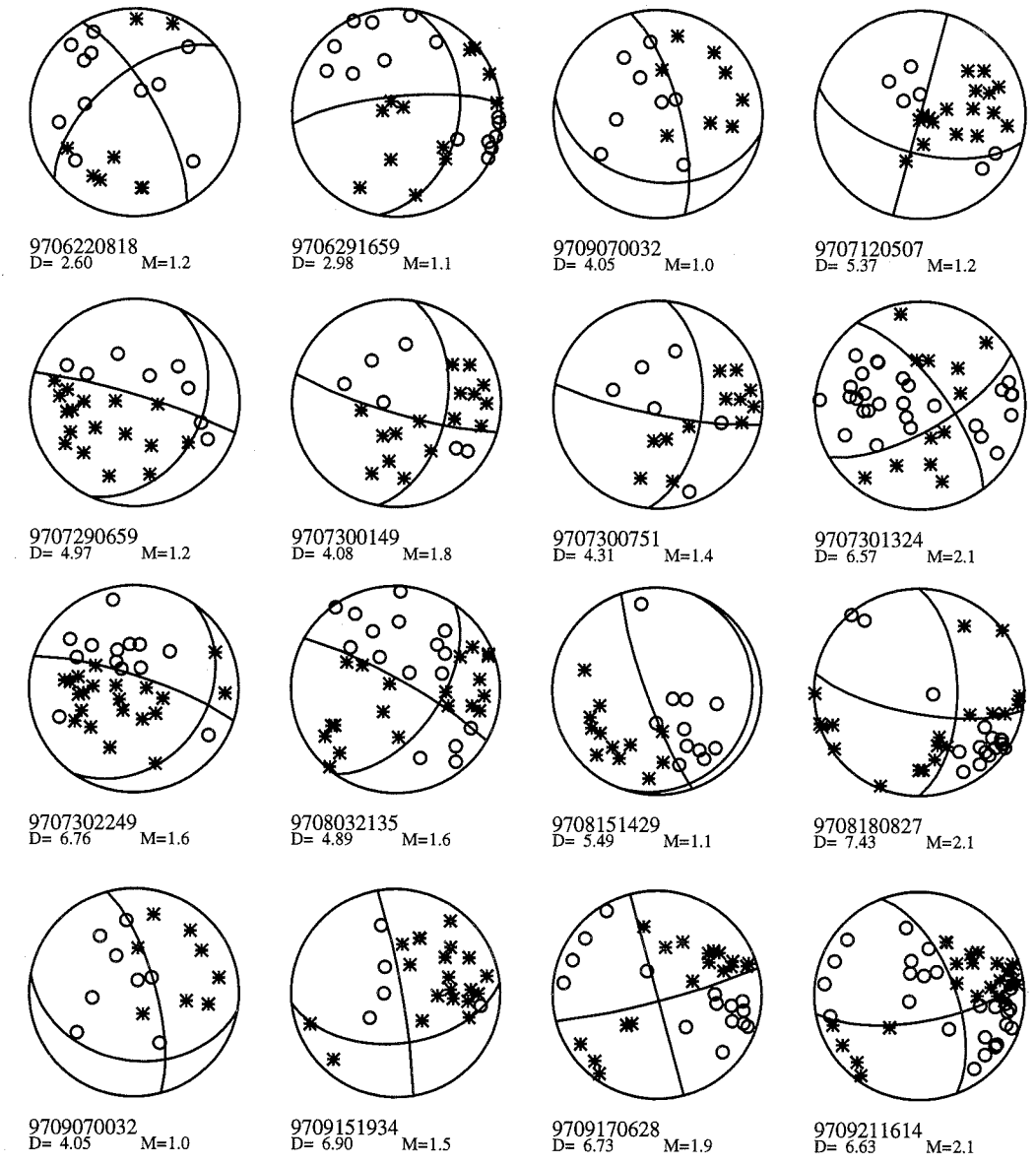
Figure 5: A random sampling of focal mechanisms from the data set of 696 earthquakes. P-wave polarities are plotted on a lower hemisphere equal-area projection. Open circles represent dilatational arrivals; Stars represent compressional arrivals. D indicates depth of the earthquake; M indicates the magnitude of the earthquake.
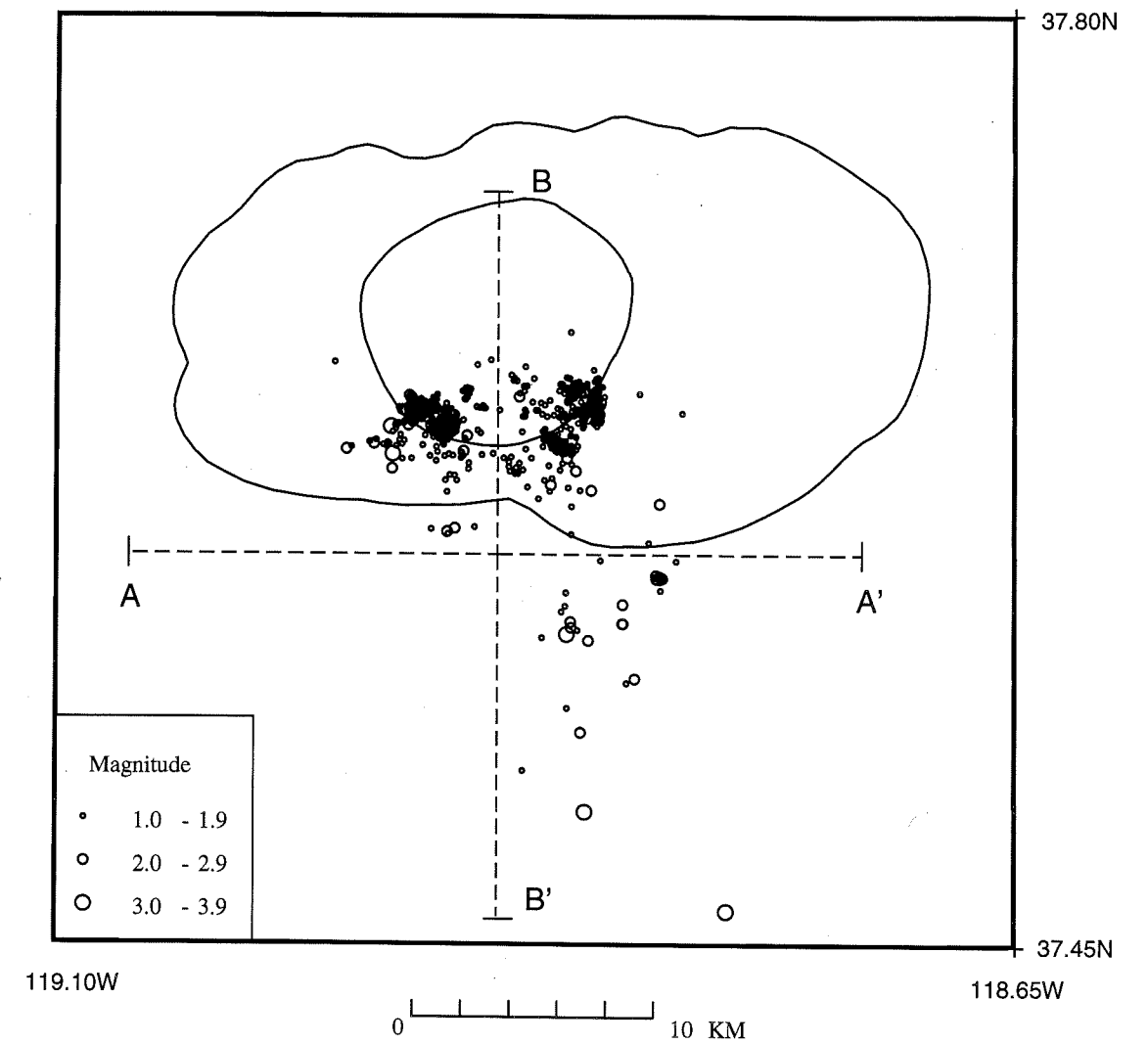
Figure 6: Map of earthquakes in the Long Valley area that have good focal mechanisms (quality 'A' or 'B'), June 1997-September 1997. The caldera and resurgent dome boundaries are outlined. Cross-sections shown in Figure 7 are indicated by the dashed lines (A-A', B-B').

(a)

(b)
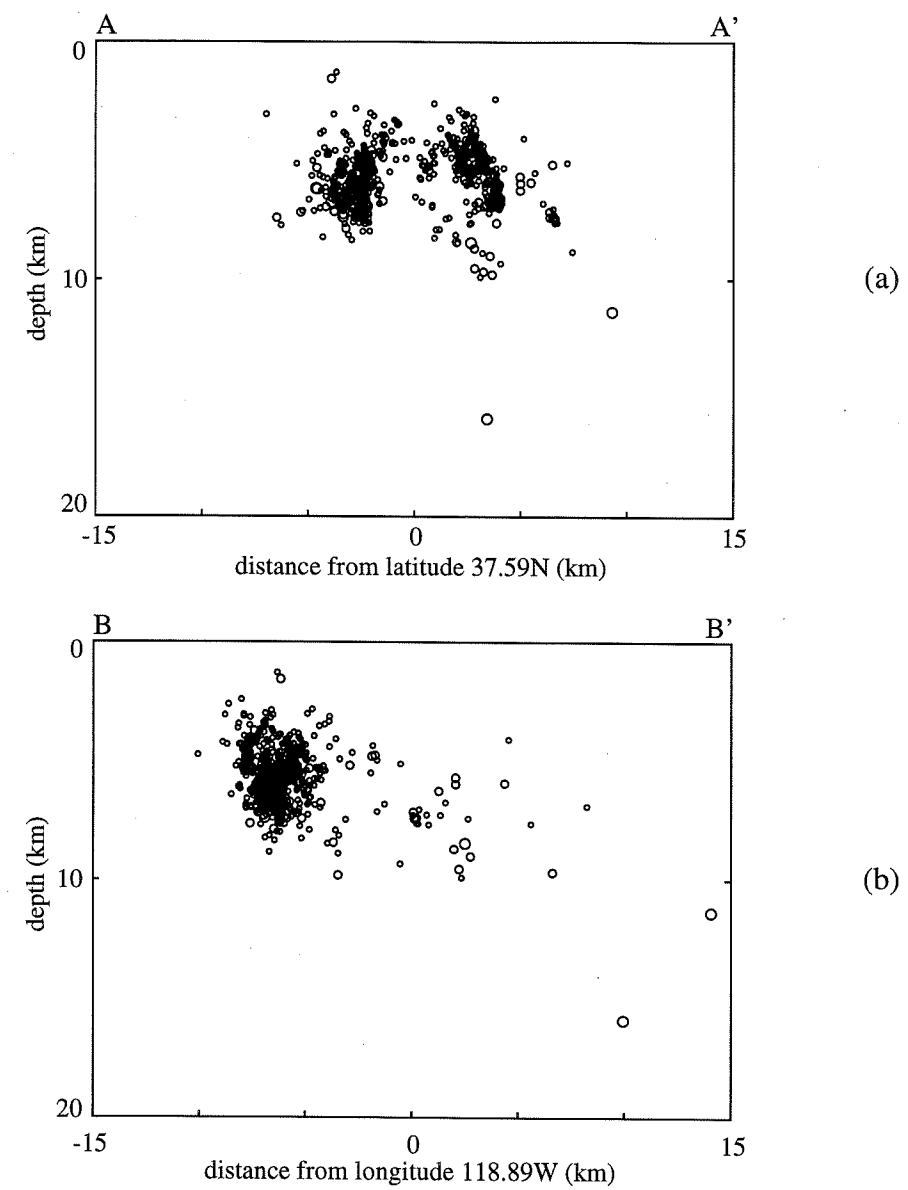
Figure 7: (a) East-west cross-section of earthquakes that have good focal mechanisms (quality 'A' or 'B'), June-September 1997. (b) North-south cross-section. A map view of these earthquakes is illustrated in Figure 6.

23

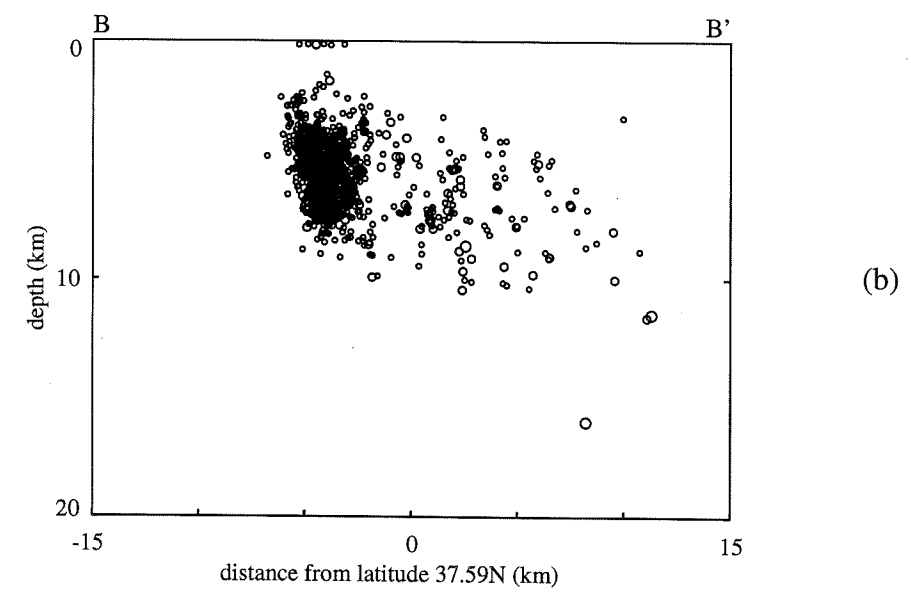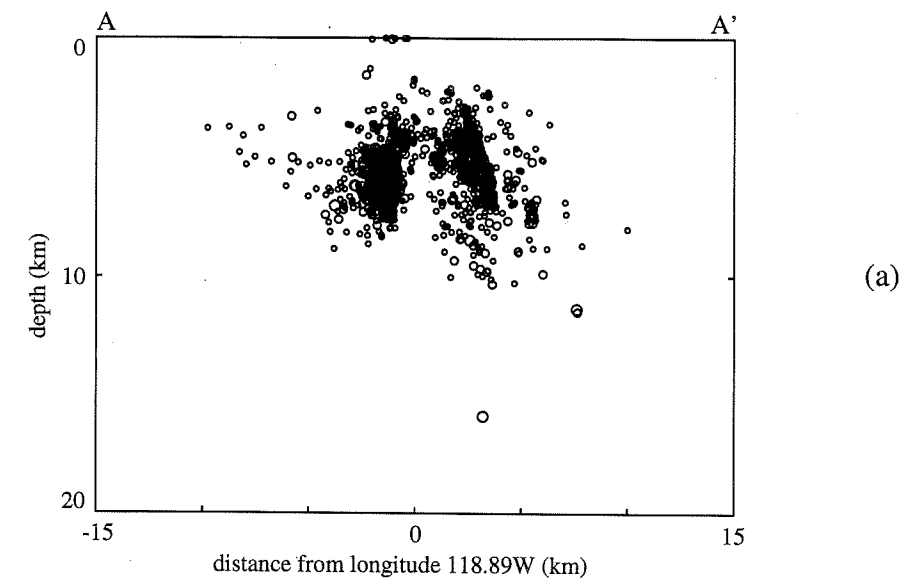

Figure 8: (a) East-west cross-section of earthquakes that have magnitudes greater than or equal to 1.0, June-September 1997. (b) North-south cross-section. A map view of these earthquakes is illustrated in Figure 1.
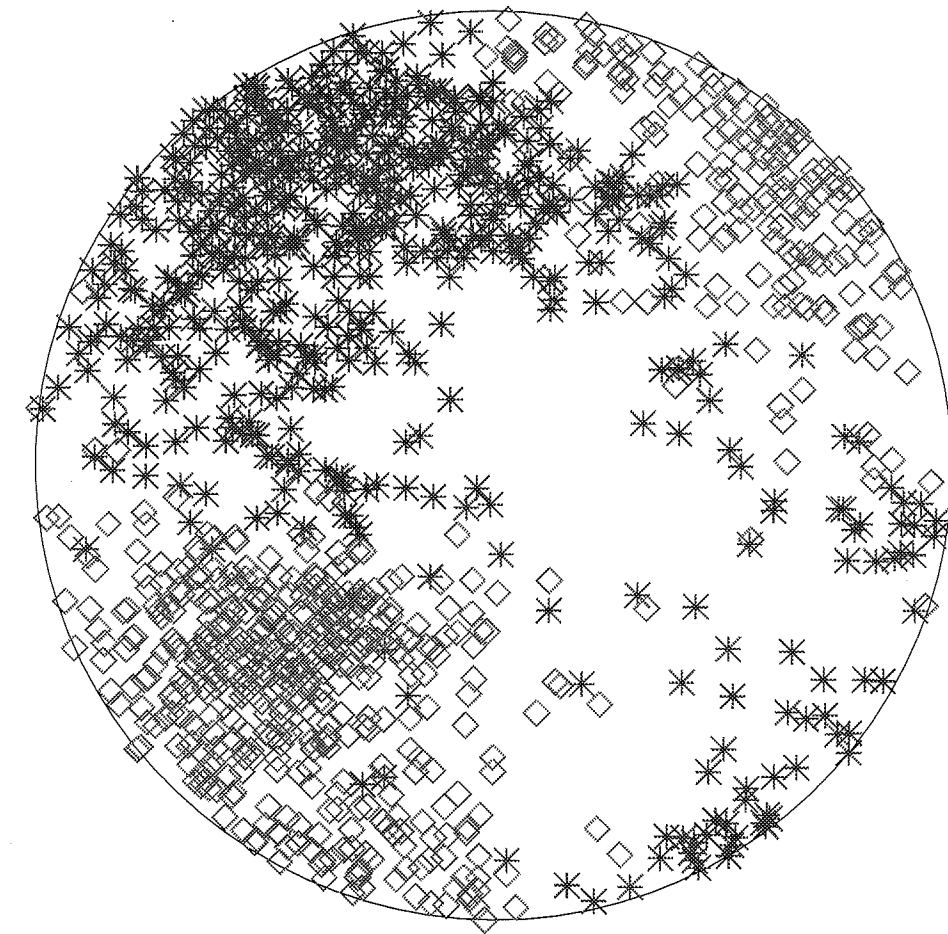
Figure 9: Lower hemisphere equal area projection of P- and T-axes of focal mechanisms in the entire data set (696 earthquakes). Stars represent P-axes; Diamonds represent T-axes.

Focal Mechanism Stress Inversion

Gephart and Forsyth's (1984) Focal Mechanism Stress Inversion program (FMSI) finds homogenous regional stress directions that best fit a population of earthquake focal mechanisms. As a forward problem, direction of maximum shear stress can be calculated along any fault plane orientation, given a uniform stress field. This shear stress direction defines the direction that slip would occur on the fault. To resolve shear stress along the fault plane, one can transform the stress tensor from the coordinate system defined by principal stress directions (X) into a coordinate system defined by the fault plane (X$'$). This rotation is accomplished by means of a transformation matrix β such that

$$\sigma_{ij}^{X'} = \beta_{ip}\beta_{jq}\sigma_{pq}^{X} \tag{1}$$

where $\underline{\sigma}$ is the stress tensor. While absolute values of the principal stresses cannot be resolved, the ratio of stresses can be expressed as

$$R = \frac{\sigma_2 - \sigma_1}{\sigma_3 - \sigma_1} = -\frac{\beta_{13}\beta_{23}}{\beta_{12}\beta_{22}} \tag{2}$$

when $X^{/}_1$ is defined to be normal to the fault plane and $X^{/}_3$ is defined to be parallel to the slip direction. σ_1 is the maximum compressive stress direction and σ_3 is the least compressive stress direction.

Given a set of focal mechanisms, providing information about both fault plane orientations and direction of slip, FMSI performs a grid search of stress directions (σ_1, σ_2, and σ_3) and R values. For each stress model tested, FMSI calculates the minimum fault plane rotation necessary to bring the slip direction into coincidence with the direction of shear stress along the plane. Initially, the misfit is determined by rotation around an axis defined by any of the principal stress directions (the approximate method). The approximate method is used to narrow the set of stress directions which may be consistent with the data, thereby significantly reducing the computer run time necessary to perform the inversion. With this smaller set, misfit is determined by rotation around an arbitrary axis, providing a better estimate of a true minimum rotation (the exact method). Because focal mechanisms cannot distinguish between fault planes and auxiliary planes, the minimum rotation is calculated separately for both the planes. The plane with the lesser rotation misfit is considered to be the fault plane, unless the user assigns an a priori fault plane orientation to the earthquake. As there is little justification for assigning a fault plane to my data, I made no a priori fault plane determinations. A confidence interval based on a one-norm minimization of the misfits is constructed, following Gephart and Forsyth (1984).

This formulation of the stress inversion problem takes into account the fact that faults which are not aligned with the present stress field may exist and may be active, but does

not address how likely it is that these faults will fail. Fault planes with negligible shear stress are not differentiated from fault planes with significant shear stress as long as the direction of maximum shear stress is coincident with the modeled shear stress along the plane.

Grid Search

The initial inversion of the data sets consisted of a search of the entire range of possible stress orientations on a 10 degree grid using the approximate method. The regions of possible solutions suggested by the approximate method were then searched more thoroughly using the exact method. This search uses a combination of grids with 5 degree and 10 degree spacing. The ratio R was searched at intervals of 0.1.

Chapter 4

Results

Inverting the entire data set for a regional stress field produces a best fit model which is an oblique strike-slip regime with σ_1 trending 315° and plunging 40°. The σ_3 axis trends 210° and plunges 17° (Table 2). For this solution, the R value is 0.5, which indicates that the magnitude of σ_2 is midway between σ_1 and σ_3. The average misfit for the best fit model is 7.5°. Solutions falling within the 95% confidence interval also allow for a pure strike-slip regime with σ_1 horizontal and σ_2 nearly vertical (Figure 10a). Acceptable R values for these models range from 0.4 to 0.6.

Is this result compatible with a uniform stress field in this region? My data set has a mean focal plane orientation uncertainty of 17°. Using synthetic data sets, Wyss et. al. 1992 determine that for a data set with focal mechanism uncertainties of 15°, a stress inversion misfit of less than 8° is consistent with a uniform stress field. Applying this result to my data set, the best fit stress orientation, and indeed any model within the 95% confidence intervals, is compatible with a uniform stress field. In addition, misfits for individual earthquakes seem well distributed spatially and temporally. Twenty earthquakes have very large misfits (i.e. misfits > 20°), a number consistent with what would be expected statistically. This result would imply that a regional stress field could be the dominant influence on earthquakes in Long Valley during summer 1997.

However, this consistency with a uniform stress model does not preclude local stress heterogeneity. The choice of fault planes made by FMSI are not necessarily the correct ones, and this ambiguity can affect the resolution of the inversion (Michael 1987, Wyss 1992). In particular, Michael (1987), shows that when two sets of focal mechanisms produced by distinct stress regimes are combined into a single data set, a low misfit can be produced for a uniform stress field model through the process of "choosing" fault planes.

One test for uniformity would be to attempt to lower the misfit using a data set which has smaller errors. Wyss et al. (1992) also determined that inversion misfit errors of less than 6° might be expected from a data set with focal mechanism errors of 10°. If the stress field were indeed homogenous throughout the study region, then the misfit between the model and the actual stress field is primarily due to errors in focal mechanism determination. As such, a data set with less error present in its focal mechanisms would produce a lower minimum misfit to the model. I selected from the entire data set focal mechanisms with quality code A (subset A). These focal mechanisms should have errors in fault plane orientation of less than 10° and therefore represent a more accurate data set. This subset consists of 132 focal mechanisms and is well distributed throughout the study area (Figure 11). The best fit from this inversion is σ_1 [trend:plunge] = 320 : 10, σ_2 = 72 : 65, and σ_3 = 226 : 23 (Figure 10b, Table 2). The solution sets overlap significantly at the 95% confidence level suggesting that these sets were likely produced in the same stress field, as one would expect.

Interestingly, although the trend of σ_1 is similar between the best fit solutions for the

entire data set and the smaller data set, their respective best fit plunges are 30° apart from each other. Given the spatial distribution of these earthquakes it is unlikely that the two data sets are sampling different proportions of separate earthquake populations. This implies the plunge of the σ_1 and σ_2 axes are not well constrained by the data set. The misfit for this best fit solution is 6.7^o, which is a slight improvement over the entire data set. However, this is not as great an improvement as would be expected based on the data quality. The fact that this misfit measurement does not decrease to less than 6° may be an indication that the stress field is not, in fact, completely uniform in this region. Alternatively, it may indicate that the errors present in the focal mechanisms are underestimated.

I chose three subsets of focal mechanisms to test the hypothesis that the stress field is spatially varying (Figure 12). I label these subsets 'east', 'west', and 'south'. These subsets do not include all the earthquakes in the data set. The east subset was determined by including any earthquakes located within a box visually drawn to contain the majority of the earthquakes associated with the earthquake clusters in the eastern section of the south moat. Likewise, the west subset was chosen to include the earthquake clusters in the western section of the south moat. The south subset contains all the earthquakes located to the south of Long Valley as well as two earthquakes located just inside the mapped caldera boundary. The western subset consists of 348 earthquakes, the eastern subset consists of 247 earthquakes, and the southern subset consists of only 37 earthquakes. The possibility that stress orientation varies with depth was explored cursorily by visually examining cross-sections for systematic differences in focal mechanisms with depth. As no pattern

could be discerned, this possibility was not pursued.

Figure 13 illustrates differences in focal mechanism P- and T-axes between these three groups. The T-axes of both the west and east subsets cluster tightly, with the T-axes of the east group tending to be closer to horizontal than the T-axes of the west group. The east P-axes are more tightly clustered than the west P-axes which tend to be more variable. In all three subsets, the P-axes predominate in the NW quadrant. P- and T-axes of the south subset are distributed similarly to the P- and T-axes of the east group.

Subset Inversions

The best fit stress orientations for these three subsets, south, west, and east, are summarized in Table 2 and Figure 14. The best fit model for the west subset is an almost horizontal σ_1 oriented NW-SE, σ_3 oriented SW, and an R value of 0.3. Models with R values of 0.1 to 0.4 are within the 95% confidence intervals. These R values indicate that σ_1 and σ_2 are closer in magnitude to each other than σ_2 and σ_3 are. The best fit model for the east subset has a σ_1 plunging 45° to the NW and a σ_3 oriented SW, with an R value of 0.5. Within the 95% confidence intervals, R varies from 0.3 to 0.7. Best fitting σ_3 orientations for both the west and east subsets are within 10° of each other. The results of the south group show σ_1 plunging 29° to the north and σ_3 plunging 25° to the W-SW; the best fitting R value is 0.7. R is not constrained for the south group and varies from 0.1 to 0.9 for models within the 95% confidence intervals.

Comparing the solution sets for the east and west subsets, while the 95% confidence intervals of σ_1 and σ_3 overlap, the 95% confidence intervals of σ_2 are distinct. Using this criteria, I conclude that the stress orientations are different between these two groups. One interpretation that can be made at this point is that the two minima found in the inversion of the entire data set reflect the different stress distributions in the western and eastern sections of the south moat, with an oblique strike slip regime in the east and a nearly pure strike-slip regime in the west. In this interpretation, σ_3 remains relatively stationary throughout the south moat, while σ_1 and σ_2 rotate around its axis.

Alternatively, a rotation in stress orientation of 15° to 20° around a vertical axis is sufficient to modestly overlap the 95% confidence interval sets of the east and west groups and can also explain the results of the stress inversion. If such a rotation occurs, then stress in the eastern section of the south-moat is oriented slightly more towards the north than that of the western south-moat. This rotation is in the opposite sense than one might expect from a physical model of a magma chamber underlying the resurgent dome contributing a radial stress superposed on the regional stress field.

The south subset, while not statistically distinguishable from either the west or the east subsets, does demonstrate a rotation in the best fit stress axes towards a more typical Basin and Range stress of east-west maximum extension, and as such this result may be real.

Fault Planes

With an objective method of determining fault planes, FMSI provides a way of

examining the tectonic structure of a region. A fault plane orientation which is consistently picked for a good stress orientation model is likely to reflect a true fault plane (Michael,1987). Long Valley is a highly complex area and it is likely that potentially active faults exist at all orientations. However, the faults which are activated depend strongly on the stress field, and the fault plane choices of FMSI may provide insight into how faulting is occurring in this region.

The first step in this endeavor is to determine which of FMSI's fault plane choices is likely to be the true fault plane. The criteria which I use is that the plane must have a misfit to the stress model of less than 15° and that its misfit must be at least 15° less than the misfit of the auxiliary plane. These values were derived from my estimates of fault plane uncertainty. I use the best fit stress orientation models for the east and west subsets to determine the likely fault planes for their respective earthquakes. The south subset does not include enough earthquakes with unambiguous fault planes to draw any meaningful conclusions, so these fault planes are not discussed.

Figure 15 illustrates the orientations of the unambiguous fault plane choices for the east and west subsets. 37% of the west subset earthquakes satisfy the criteria for unambiguous fault planes while 50% of the east subset satisfy the criteria. The west group seems to be an intermixture of two basic orientations of fault planes. One is a NW-SE oriented steeply dipping fault with both right-lateral and normal motion along the fault. The other is a NE-SW oriented shallow dipping fault with predominantly left-lateral motion. The right-lateral NW-SE oriented faults are consistent with geodetic studies of previous south moat swarms (Cockerham and Savage, 1984) which demonstrate

predominantly right-lateral motion in this area. In the east group, fault plane orientation seems closely correlated with earthquake clustering. As shown in Figure 15, there is a distinct change from E-W right-lateral strike-slip faulting in the south of the subset area to N-S left-lateral strike-slip faulting in the east. The consistency with which these planes are picked within the earthquake clusters lends credence to the supposition that these are separate tectonic features. Unlike the earthquakes in the west subset and those in the south of the east subset, the left-lateral earthquakes in the northeast of the east subset appear to be unrelated to the south moat right-lateral zone. They also do not appear to be associated with regional faulting in the area, having a different strike and sense of motion than the regional Sierran normal faults. It is unclear how these faults relate to the structure of the caldera.

Table 2: Best fit solutions to stress inversions

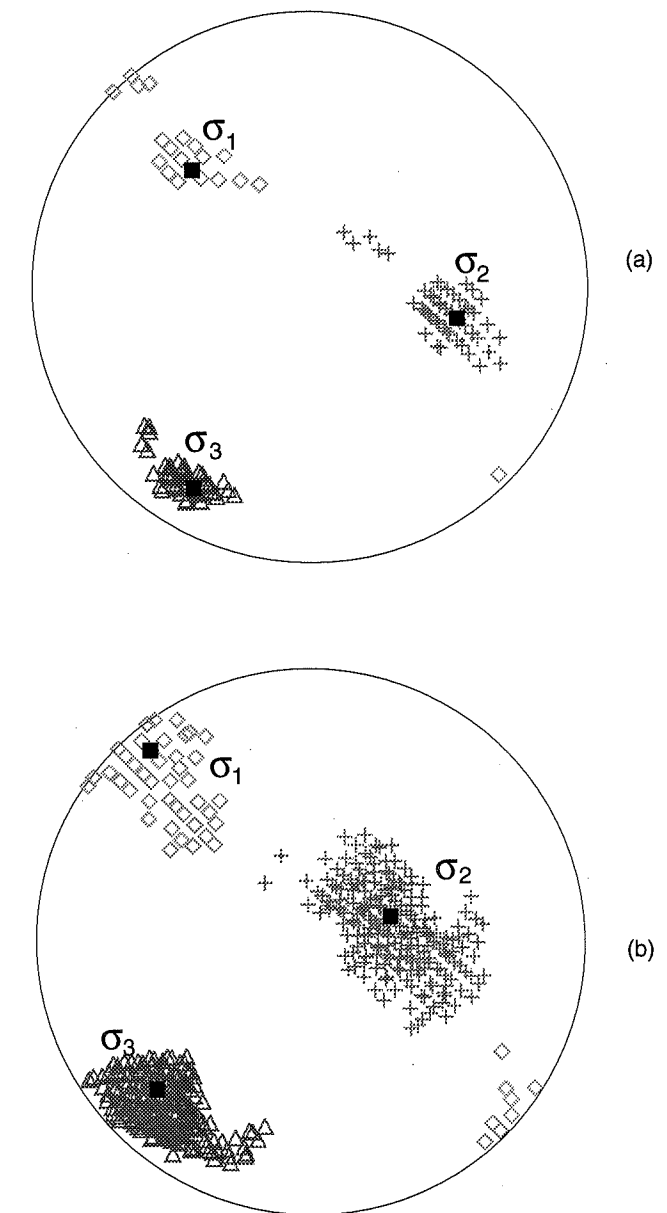|	number of earthquakes	σ_1 (trend: plunge)	σ_2 (trend: plunge)	σ_3 (trend: plunge)	ratio R	misfit (°)
all	696	315:40	102:45	210:17	0.5	7.5
A	132	320:10	72:65	226:23	0.4	6.6
west	348	129:5	25:70	221:19	0.3	6.4
east	247	319:45	219:10	219:10	0.5	6.5
south	37	354:29	249:25	249:25	0.7	5.5

Figure 10: Results of stress inversion plotted on a lower hemisphere equal area projection. (a) solutions within the 95% confidence interval for the entire data set. (b) solutions within the 95% confidence intervals for subset A. Diamonds represent σ_1 solutions. Plus marks represent σ_2 solutions. Triangles represent σ_3 solutions. Squares indicate best fit solutions for σ_1, σ_2, and σ_3.
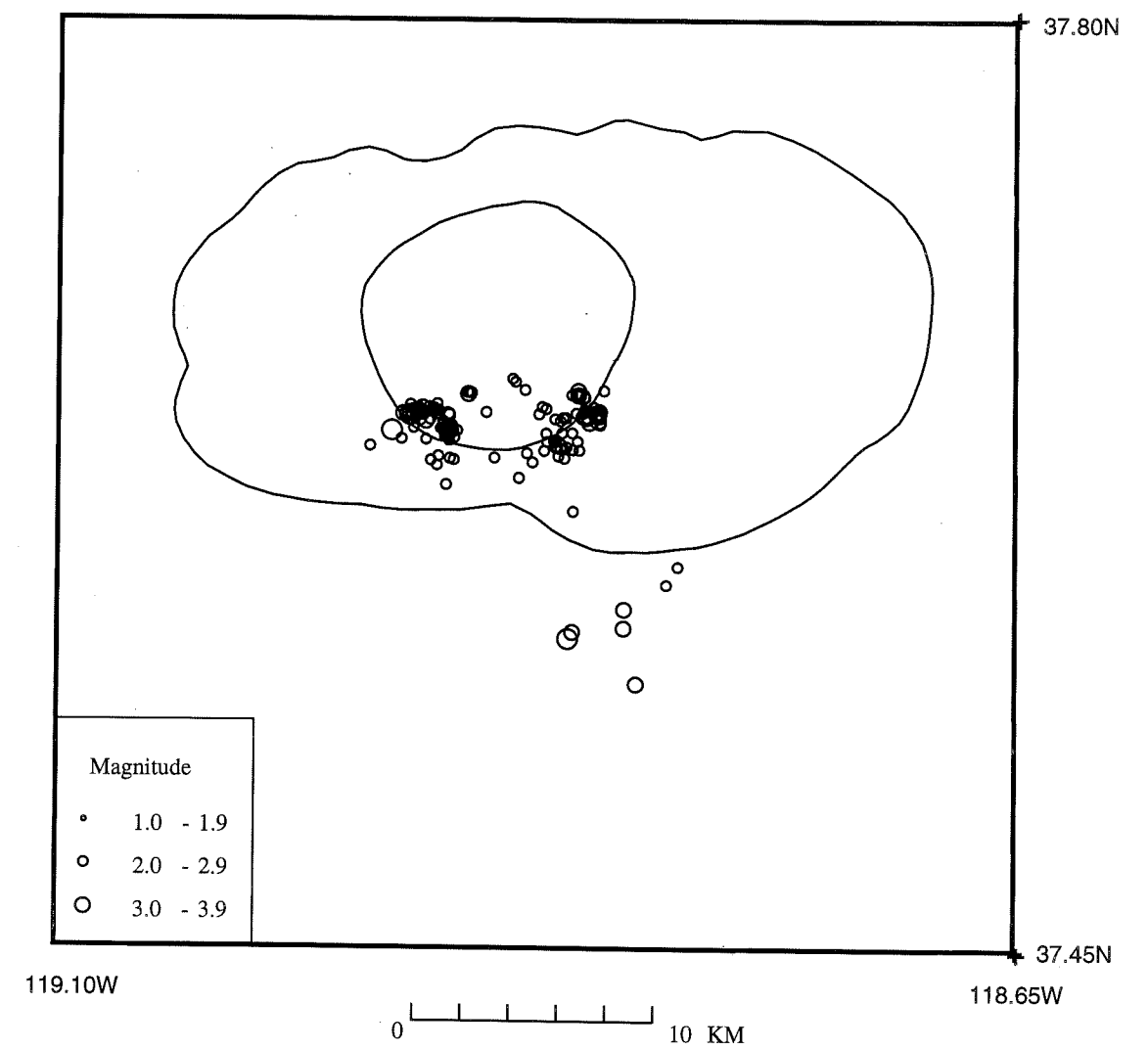
Figure 11: Map of earthquakes that have quality A focal mechanisms (132 earthquakes, subset A).
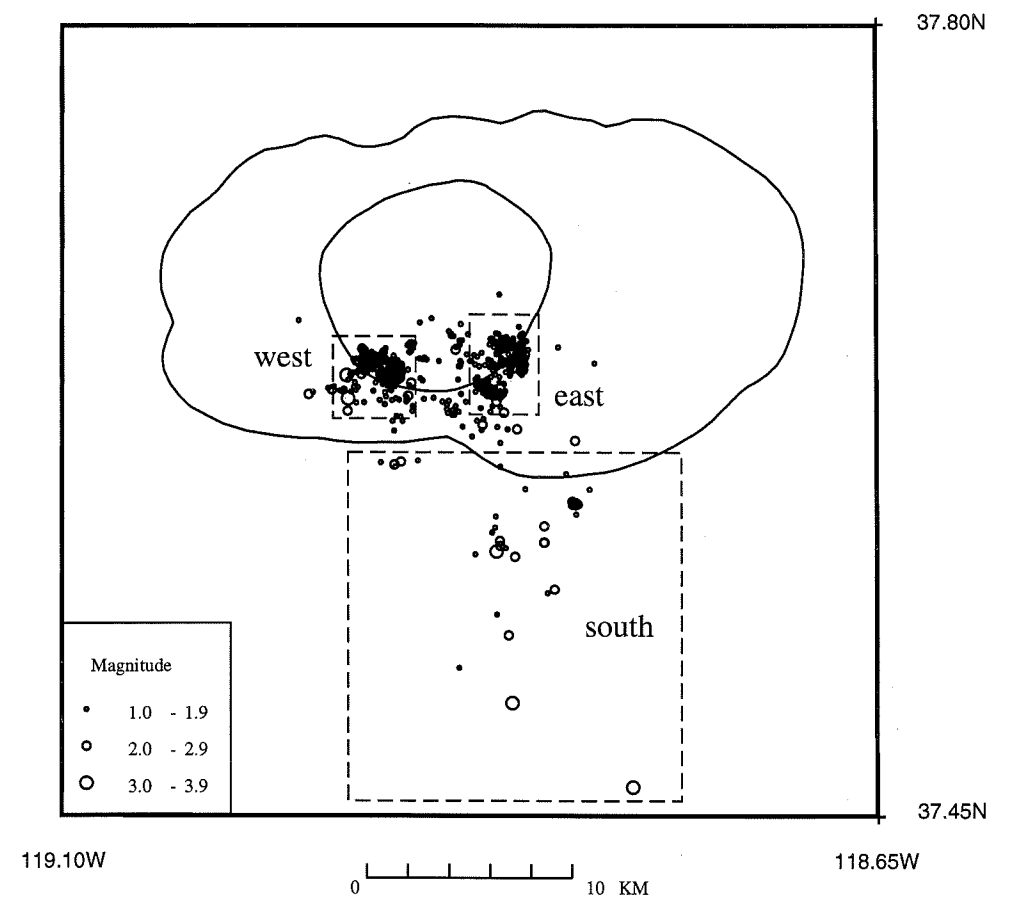
Figure 12: Map of subsets. Dashed boxes define east, west, and south subsets.
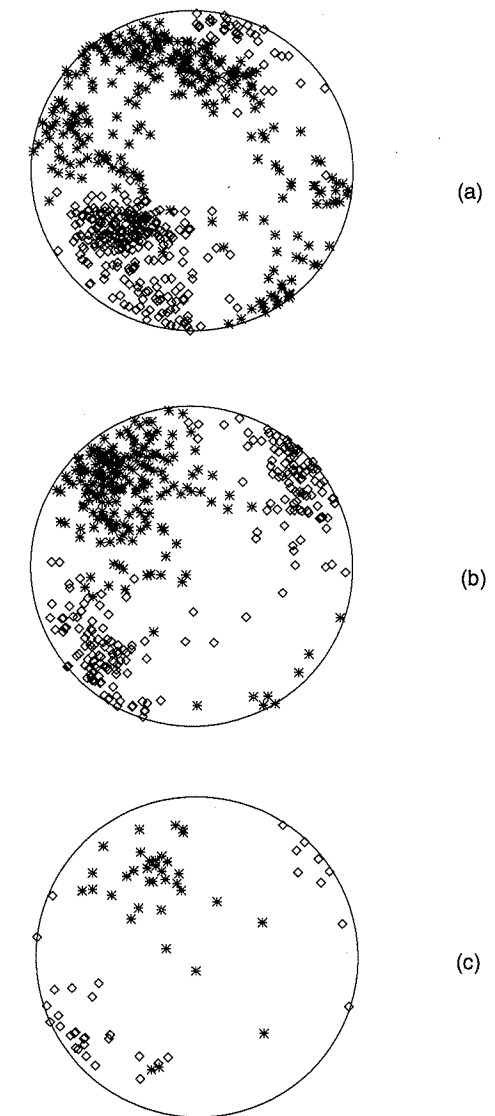
(a)

(b)

(c)

Figure 13: Lower hemisphere equal area projection of P- and T-axes. (a) P- and T-axes of earthquakes in the west subset. (b) east subset. (c) south subset. Symbols are the same as in Figure 9.
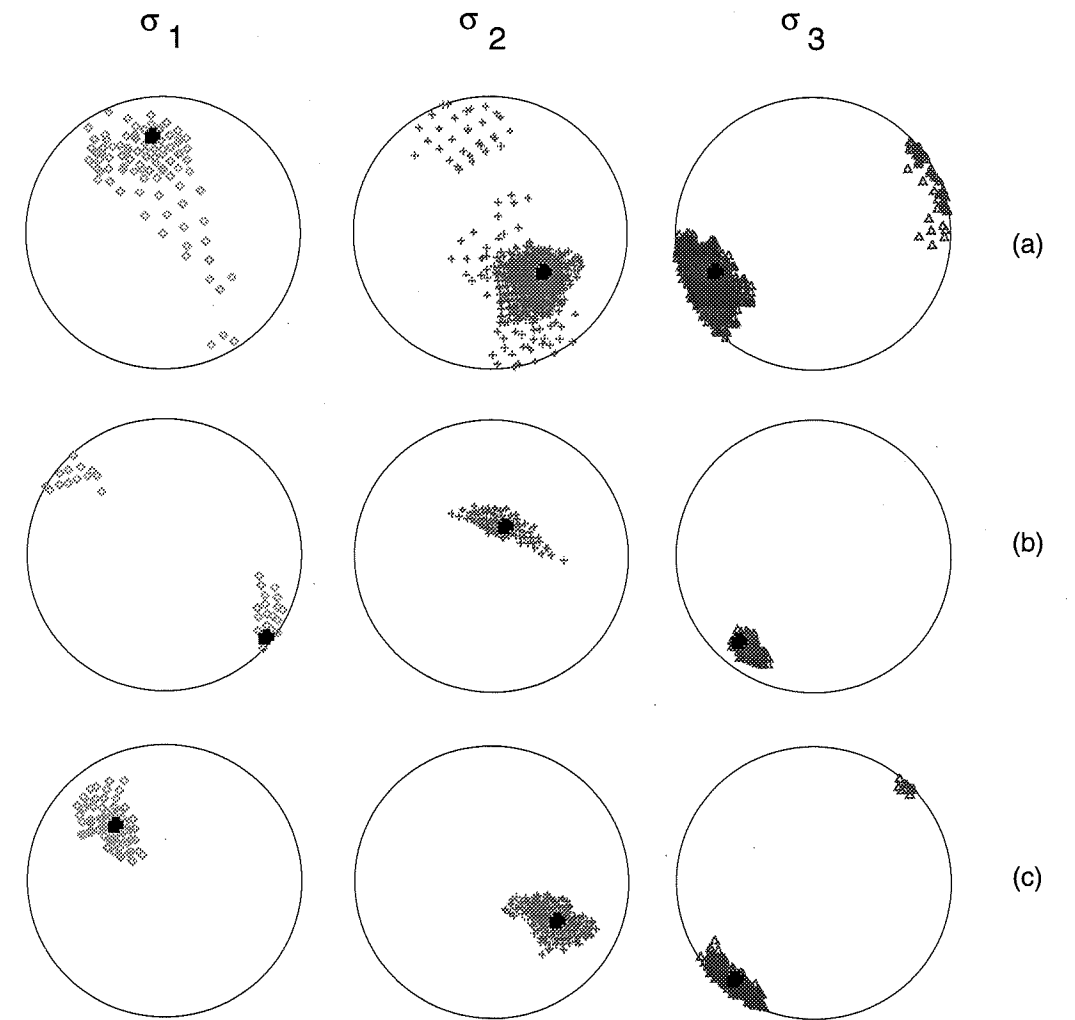
Figure 14: Stress inversion results plotted on a lower hemisphere equal area projection for subsets (a) south. (b) west. (c) east. σ_1, σ_2, and σ_3 solutions within the 95% confidence intervals are plotted separately. Solid squares show the best fit solutions for σ_1, σ_2, and σ_3.
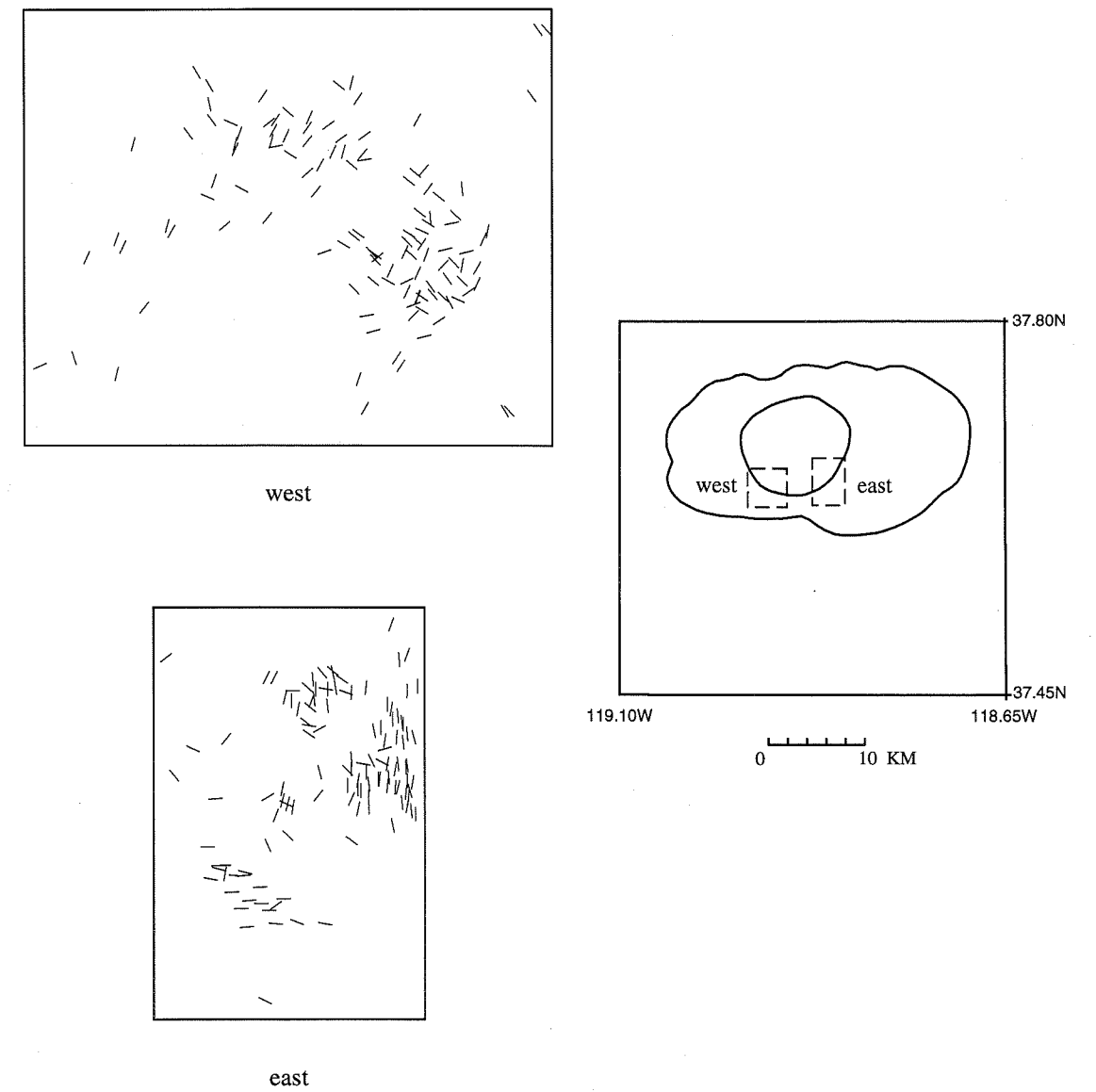
west

east

Figure 15: Map of fault plane strikes for the east and west subsets. These fault planes satisfy the criteria that they have an individual misfit of less than 15° to their repective best fit stress orientation models for the east and west subsets and that their misfit is at least 15° less than the misfit of the auxiliary plane.

Chapter 5

Conclusion

Long Valley caldera is a complex region where regional stresses play a large role in earthquake activity. While the overall picture of SW extension and NW compression are consistent with previous estimates of stress orientation in the south moat of Long Valley caldera (Moos and Zoback, 1993), statistically significant differences in stress orientation are found between subgroups of earthquakes in the south moat. However, these differences are not easily attributable to an expanding magma chamber beneath the central resurgent dome. While it is likely that the magmatic system plays a role in the process of earthquake swarm initiation, as implied by the temporal relationship between deformation and earthquake swarm activity (Langbein, 1995), it does not make a large contribution to the stress field in the south moat. A magmatic 'triggering' of the swarms remains a possibility, and one may speculate that processes such as loading of faults which are close to failure or heating of pore fluids may be possible mechanisms of swarm induction which do not require large stresses from the magma system.

List of References

Bailey, R.A., Geologic map of Long Valley caldera, Mono-Inyo craters volcanic chain and vicinity, Mono county, California, *U.S. Geological Survey Misc. Invest. Map I-1933*, 1989.

Bailey, Roy A., C. Dan Miller, and Kerry Sieh, Excursion 13B: Long Valley caldera and Mono-Inyo craters volcanic chain, eastern California, *New Mexico Bureau of Mines and Mineral Resources Memoir 47*, 1989.

Bailey, R.A., G.B. Dalrymple, and M.A. Lanphere., Volcanism, structure, and geochronology of Long Valley caldera, Mono County, California, *J. Geophys. Res.*, *81*,725-744, 1976.

Denlinger, Roger P., Francis S. Riley, James K. Boling, and Michael C. Carpenter, Deformation of Long Valley caldera between August 1982 and August 1983, *J. Geophys. Res.*, *90*, 11199-11209, 1985.

Estrem, J.E., M. Lisowski, and J.C. Savage, Deformation in the Long Valley caldera, California, 1983-1984, *J. Geophys. Res.*, *90*, 12683-12690, 1985.

Farrar, C.D., M.L. Sorrey, W.C. Evans, J.F. Howle, B.D. Kerr, B.M. Kennedy, C.Y. King, and J.R. Southon, Forest-filling diffuse CO_2 emission at Mammoth Mountain as a sign of magmatic unrest, *Nature*, *376*, 675-678, 1995.

Fink, J.H., Geometry of silicic dikes beneath the Inyo domes, California, *J. Geophys. Res.*, *90*, 11127-11134, 1985.

Gephart, John W., and Donald W. Forsyth, An improved method of determining the regional stress tensor using focal mechanism data: application to the San Fernando earthquake sequence, *J. Geophys. Res.*, *89*, 9305-9320, 1984.

Gillard, Dominique, Max Wyss, and Paul Okubo, Type of faulting and orientation of stress and strain as a function of space and time in Kilauea's south flank, Hawaii, *J. Geophys. Res.*, *101*, 16025-16042, 1996.

Hill, D.P., W.L. Ellsworth, M.J.S. Johnston, J.O. Langbein, D.H. Oppenheimer, A.M. Pitt, P.A. Reasenberg, M.L. Sorrey, and S.R. McNutt, The 1989 earthquake swarm beneath Mammoth Mountain, California: an initial look at the 4 May through 30 September activity, *Bull. Seis. Soc. America*, *80*, 325-339, 1990.

Hill, D.P., E. Kissling, J.H. Luetgert, U. Kradolfer, Constraints on the upper crustal structure of the Long Valley-Mono Craters volcanic complex, eastern California, from seismic refraction measurements, *J. Geophys. Res.*, *90*, 11135-11150, 1985b.

Julian, Bruce R., and Stuart A. Sipkin, Earthquake processes in the Long Valley caldera area, California, *J. Geophys. Res.*, *90*, 11155-11169, 1985.

Langbein, John, Daniel Dzurisin, Grant Marshall, Ross Stein, and John Rundle, Shallow and peripheral volcanic sources of inflation revealed by modeling two-color geodimeter and leveling data from Long Valley caldera, California, 1988-1992, *J. Geophys. Res.*, *100*, 12487-12495, 1995.

Langbein, John, David P. Hill, Timothy N. Parker, and Stuart K. Wilkinson, An episode of reinflation of the Long Valley Caldera, Eastern California, *J. Geophys. Res.*, *98*, 15851-15870, 1993.

Langbein, John, Deformation of the Long Valley caldera, Eastern California from mid-1983 to mid-1988: measurements using a two-color geodimeter, *J. Geophys. Res.*, *94*, 3833-3849, 1989.

Michael, Andrew Jay, Use of focal mechanisms to determine stress: a control study, *J. Geophys. Res.*, *92*, 357-368, 1987.

Miller, C.D., Holocene eruptions at the Inyo volcanic chain, California: implications for possible eruptions in the Long Valley caldera, *Geology*, *13*,14-17, 1985.

Moos, Daniel, and Mark D. Zoback, State of stress in Long Valley caldera, California, *Geology*, *21*, 837-840, 1993.

Newhall, Christopher G, and Daniel Dzurisin, Historical Unrest at Large Calderas of the World, *U.S. Geological Survey Bulletin 1855*, 1988.

Reasenberg, P., and D. Oppenheimer, FPFIT, FPPLOT, and FPPAGE: Fortran computer programs for calculating and displaying earthquake fault-plane solutions, *Open-File Report No. 85-0739*, 1985.

Rundle, John B., and David P. Hill, The geophysics of a restless caldera- Long Valley, California, *Ann. Rev. Earth Planet. Sci.*, *16*, 251-271, 1988.

Rundle, John B., and James H. Whitcomb, A model for deformation in Long Valley, California, 1980-1983, *J. Geophys. Res.*, *89*, 9371-9380, 1984.

Savage, J.C., R.S. Cockerham, J.E. Estrem, and L.R. Moore, Deformation near the Long Valley caldera, eastern California, 1982-1986, *J. Geophys, Res.,* *92*, 2721-27746, 1987.

Savage, J.C., and R.S. Cockerham, Earthquake swarm in Long Valley caldera, California, January 1983: evidence for dike inflation, *J. Geophys. Res.,* *89*, 8315-8324, 1984.

Sieh, K., and M. Bursik, Most recent eruption of the Mono Craters, east-central California, *J. Geophys. Res.,* *91*, 12539-12571, 1986.

Wu, M., and H. F. Wang, Deformations and inferred stress field for ellipsoidal sources at Long Valley, California, 1975-1982, *J. Geophys. Res.,* *93*, 13285-13296, 1988.

Wyss, Max, Beiyuan Liang, W.R. Tanigawa, and Xiaoping Wu, Comparison of orientations of stress and strain tensors based on fault plane solutions in Kaoiki, Hawaii, *J. Geophys. Res.,* *97*, 4769-4790, 1992.